Finite-Element Domain Decomposition Methods for Analysis of Large-Scale Electromagnetic Problems

Ming-Feng Xue and Jian-Ming Jin

Department of Electrical and Computer Engineering
University of Illinois at Urbana-Champaign, Urbana, Illinois 61801, USA
xue6@illinois.edu, j-jin1@illinois.edu

Abstract ─ This paper presents an overview of our recent development of domain decomposition methods for finite element analysis of large-scale electromagnetic problems. More specifically, it presents several domain decomposition algorithms based on the Dual-Primal Finite Element Tearing Interconnecting (FETI-DP) method for solving vector wave equations. These algorithms expand the capability and improve the performance of the FETI-DP method by: (1) lifting the requirement of conformal meshes on subdomain interfaces, (2) speeding up the convergence of the iterative solution of the global interface problem, and (3) incorporating appropriate truncation boundaries for more accurate simulation. Numerical results are presented to demonstrate the application, accuracy, efficiency, and capability of these algorithms.

Index Terms ─ Domain Decomposition Method (DDM), Dual-Primal Finite Element Tearing and Interconnecting (FETI-DP), Finite Element Method (FEM), higher-order transmission condition.

I. INTRODUCTION

Full-wave electromagnetic simulation has been widely used for analysis, design, and optimization in modern electrical and electronic engineering. Several Computational Electromagnetics (CEM) techniques, such as the Finite Element Method (FEM), the Method of Moments (MoM), and the Finite-Difference Time-Domain (FDTD) method, have made great progress during the past few decades [1]. Nevertheless, the scope and application of these rigorous numerical tools are still limited by the problem size and complexity, for which computation time and computer memory requirements become excessive. A popular solution is to develop a Domain Decomposition Method (DDM), which is a numerical approach that decomposes a large-scale simulation problem into many small subdomain problems that can be computed simultaneously with parallel processors [2-4]. The combination of the DDM and the FEM is much more efficient than that of the DDM and the MoM because the FEM involves only local interaction. With the use of unstructured meshes and curvilinear elements, the FEM is much better at modeling curved surfaces, fine structures, and composite materials than does the FDTD. As a result, the FEM-based DDMs have attracted the most attention among all the DDMs.

The FEM-based DDMs can be categorized into two groups: one based on the Schwarz method and the other based on the Schur complement method. Among a variety of Schur complement DDMs [2], the Dual-Primal Finite Element Tearing and Interconnecting (FETI-DP) method, developed by Farhat, et al. [5-9], shows excellent numerical scalability and parallel efficiency. When first introduced to CEM, the FETI-DP method assumed an unknown Neumann boundary condition on a subdomain interface with the aid of one Lagrange multiplier [10]. It was a typical nonoverlapping iterative substructuring DDM. Later, an unknown Robin boundary condition was introduced on the subdomain interface with the aid of two Lagrange multipliers to improve the convergence of the global interface iterative solution for high-frequency applications [11,12]. Both FETI-DP versions construct a global corner system that relates the fields at the crosspoints

Submitted On: February 28, 2014
Accepted On: September 24, 2014

between the subdomains through a Dirichlet continuity condition. This corner system provides a coarse grid correction to speed up the convergence of the global interface iterative solution by propagating residual errors over the entire computational domain in each iteration.

The FETI-DP algorithms developed in [10,11] require a conformal interface mesh, which means that two neighboring subdomains must have the same surface mesh at their interface. Although this requirement is naturally satisfied in applications where a global mesh is generated first for the entire domain and then decomposed into many subdomain meshes, it is hard to achieve when the entire domain is very large so that one has to first break it into small subdomains and then mesh each subdomain individually. In such a case, two neighboring subdomains usually have different surface meshes at their interface. To handle such nonconformal interface meshes, one has to introduce two sets of unknown variables and develop special DDMs to couple the solution in the adjacent subdomains [13-18].

As another important DDM, the Optimized Schwarz Method (OSM) optimizes transmission conditions on subdomain interfaces to speed up the iterative convergence for solving the global interface problem [19-21]. To derive optimized higher-order transmission conditions for vector electromagnetic fields, one surface curl-curl term related to the interface electric field and another gradient that corresponds to the interface surface charge density were proposed to ensure the convergence of both Transverse-Electric (TE) and Transverse-Magnetic (TM) evanescent modes, respectively [22-28]. Similar ideas can be found in the development of higher-order Absorbing Boundary Conditions (ABCs) in early publications [29-31]. As can be expected, this idea of using a higher-order transmission condition can also benefit the FETI-DP method formulated with two Lagrange multipliers.

For some real-life engineering problems, it is neither necessary nor desirable to mesh a computational domain together. For example, in the Computer Aided Design (CAD) of electronic devices, it is often the case that only a portion of the entire device has to be redesigned repeatedly to achieve an optimal performance [32]. Therefore, this portion has to be re-meshed multiple times, whereas the mesh for the remaining portion can be kept the same. Therefore, there is an engineering need for a DDM that can allow the user to generate meshes for different regions separately based on geometrical features and then decompose each mesh independently using an automatic mesh decomposer. With such a process, the entire computational domain may contain conformal interfaces (generated by a mesh decomposer) and nonconformal interfaces between different regions partitioned before mesh generation. For such an application, it is necessary to develop an effective DDM to deal with mixed conformal/nonconformal multi-region meshes [33,34].

This paper presents a brief overview of our recent development of FETI-DP methods for FEM analysis of large-scale electromagnetic problems. The rest of this paper is organized as follows. In Sections II.A and II.B, we first extend the conformal Lagrange Multiplier (LM)-based FETI-DP method to the case with nonconformal interface and corner meshes. Then, we consider the TE Second-Order Transmission Condition (SOTC-TE) to significantly improve the iterative convergence of the interface solution in Section II.C. Afterwards, we discuss a hybrid method and a general crosspoint correction technique in Section II.D for an efficient modeling of multi-region problems. Finally, we present several antenna radiation and wave propagation examples to demonstrate the accuracy and efficiency of the proposed solvers in Section III.

II. FORMULATION

In this section, we first review the formulation of the nonconformal LM-based FETI-DP method, then incorporate the SOTC-TE into the dual-primal framework, and finally discuss the hybrid FETI/FETI-DP scheme.

A. FETI-DP for nonconformal interface and conformal corner meshes

Assume that the entire computational domain V is first divided into N_s nonoverlapping subdomains. The problem for the sth subdomain is defined by the second-order curl-curl equation:

$$\nabla\times(\mu_r^{-1}\nabla\times\mathbf{E}^s)-k_0^2\varepsilon_r\mathbf{E}^s=-jk_0Z_0\mathbf{J}^s_{\text{imp}} \text{ in } V_s, \quad (1)$$

and the Robin boundary condition:

$$\hat{n}^s\times(\mu_r^{-1}\nabla\times\mathbf{E}^s)+\alpha^s\hat{n}^s\times(\hat{n}^s\times\mathbf{E}^s)=\mathbf{\Lambda}^s \text{ on } S_s, \quad (2)$$

where k_0 and Z_0 are the free-space wavenumber and intrinsic impedance, respectively, $\mathbf{J}^s_{\text{imp}}$ is an

impressed current, $\hat{n}^s$ is the outward normal unit vector of the sth subdomain, α^s is a complex parameter chosen to make the subdomain problem well posed, and $\mathbf{\Lambda}^s$ is an unknown variable defined on the subdomain interface. For the portion of the subdomain boundary S_s coinciding with the exterior surface of the computational domain S_0, we can either apply an ABC, a Perfectly Matched Layer (PML), or a Boundary Integral (BI) equation to the field.

To formulate the boundary-value problem defined in (1) and (2) using the FEM, the subdomain is discretized into finite elements such as tetrahedra. The vector electric field within each subdomain can then be expanded with hierarchical vector basis functions such that $\mathbf{E}^s = \{\mathbf{N}^s\}^{\mathrm{T}}\{E^s\}$ [35]. By applying Galerkin's method, the FEM equation for the sth subdomain can be derived as:

$$\begin{bmatrix} K_{ii}^s & K_{ib}^s & K_{ic}^s \\ K_{bi}^s & K_{bb}^s + M_{bb}^s & K_{bc}^s \\ K_{ci}^s & K_{cb}^s & K_{cc}^s \end{bmatrix} \begin{Bmatrix} E_i^s \\ E_b^s \\ E_c^s \end{Bmatrix} = \begin{Bmatrix} f_i^s \\ f_b^s \\ f_c^s \end{Bmatrix} - \begin{Bmatrix} 0 \\ B_{bb}^s \lambda_b^s + L_{bc}^s E_c^s \\ \lambda_c^s \end{Bmatrix}, \quad (3)$$

where

$$[K_{uv}^s] = \iiint_{V_s} [\mu_r^{-1} (\nabla \times \mathbf{N}_u^s)(\nabla \times \mathbf{N}_v^s) - k_0^2 \varepsilon_r \mathbf{N}_u^s \mathbf{N}_v^s] dV \quad (u, v = i, b, c),$$

$$\{f_u^s\} = -jk_0 Z_0 \iiint_{V_s} \mathbf{N}_u^s \mathbf{J}_{\mathrm{imp}}^s dV \quad (u = i, b, c),$$

$$[M_{bb}^s] = \iint_{S_s} \alpha^s (\hat{n}^s \times \mathbf{N}_b^s)(\hat{n}^s \times \mathbf{N}_b^s) dS,$$

$$[B_{bb}^s] = \iint_{S_s} \mathbf{N}_b^s \mathbf{N}_b^s dS,$$

$$[L_{bc}^s] = \iint_{S_s} \alpha^s (\hat{n}^s \times \mathbf{N}_b^s)(\hat{n}^s \times \mathbf{N}_c^s) dS,$$

$$\{\lambda_c^s\} = -jk_0 Z_0 \iint_{S_s} \mathbf{N}_c^s (\hat{n}^s \times \mathbf{H}) dS.$$

Different from the conformal FETI-DP method [10,11], the dual unknown $\mathbf{\Lambda}^s$ here is explicitly expanded in terms of a set of curl-conforming vector basis functions defined on S_s such that $\mathbf{\Lambda}^s = \{\mathbf{N}_b^s\}^{\mathrm{T}}\{\lambda^s\}$. Therefore, $[B_{bb}^s]$ is no longer a Boolean matrix. By using the subscripts i, b, and c, each vector is partitioned into three parts, which are associated with the interior, interface, and corners of the subdomain, respectively. The separation of the corner unknowns is one of the most important features of the dual-primal idea. Equation (3) can be written in a compact form as:

$$\begin{bmatrix} K_{rr}^s & K_{rc}^s \\ K_{cr}^s & K_{cc}^s \end{bmatrix} \begin{Bmatrix} E_r^s \\ E_c^s \end{Bmatrix} = \begin{Bmatrix} f_r^s \\ f_c^s \end{Bmatrix} - \begin{Bmatrix} [R_{br}^s]^{\mathrm{T}} (B_{bb}^s \lambda_b^s + L_{bc}^s E_c^s) \\ 0 \end{Bmatrix}, \quad (4)$$

where

$$[K_{rr}^s] = \begin{bmatrix} K_{ii}^s & K_{ib}^s \\ K_{bi}^s & K_{bb}^s + M_{bb}^s \end{bmatrix}, \quad [K_{rc}^s] = \begin{bmatrix} K_{ic}^s \\ K_{bc}^s \end{bmatrix},$$

$$[K_{cr}^s] = [K_{ci}^s \ K_{cb}^s] = [K_{rc}^s]^{\mathrm{T}},$$

$$\{E_r^s\} = \begin{Bmatrix} E_i^s \\ E_b^s \end{Bmatrix}, \text{ and } \{f_r^s\} = \begin{Bmatrix} f_i^s \\ f_b^s \end{Bmatrix}.$$

With the aid of a Boolean matrix $[R_{br}^s]$, which extracts the interface electric field $\{E_b^s\}$ out of $\{E_r^s\}$, we obtain the system equation for the dual unknowns from the first equation of (4) as:

$$\{E_b^s\} = [R_{br}^s]\{E_r^s\} = [R_{br}^s][K_{rr}^s]^{-1} \Big(\{f_r^s\} - [R_{br}^s]^{\mathrm{T}} [B_{bb}^s]\{\lambda_b^s\} - ([K_{rc}^s] + [R_{br}^s]^{\mathrm{T}} [L_{bc}^s])\{E_c^s\} \Big). \quad (5)$$

From the second equation of (4), another system equation can be derived for the primal unknowns, which is:

$$\Big([K_{cc}^s] - [K_{cr}^s][K_{rr}^s]^{-1}([K_{rc}^s] + [R_{br}^s]^{\mathrm{T}}[L_{bc}^s])\Big)[B_c^s]\{E_c\} = \{f_c^s\} - \{\lambda_c^s\} - [K_{cr}^s][K_{rr}^s]^{-1}\{f_r^s\} + [K_{cr}^s][K_{rr}^s]^{-1}[R_{br}^s]^{\mathrm{T}}[B_{bb}^s]\{\lambda_b^s\}, \quad (6)$$

where the Boolean matrix $[B_c^s]$ is introduced to extract the local corner unknowns from the global corner unknowns, which can be expressed mathematically as $[B_c^s]\{E_c\} = \{E_c^s\}$. Assembling (6) through all subdomains yields a global corner-related finite element system, which will be discussed later. It is important to note that $\{\lambda_c^s\}$ of all subdomains are cancelled out after the global assembly due to the Neumann continuity condition.

Next, we introduce the global boundary unknown vector $\{\lambda_b\}$ and the Boolean projection matrix $[Q^s]$ to extract $\{\lambda_b^s\}$ from $\{\lambda_b\}$ such that $\{\lambda_b^s\} = [Q^s]\{\lambda_b\}$, as defined in [11]. In order to obtain the global interface equation, we make use of the First-Order Transmission Condition (FOTC) on the subdomain interfaces:

$$\begin{cases} \mathbf{\Lambda}_b^s + \mathbf{\Lambda}_b^q = (\alpha^s + \alpha^q)\hat{n}^q \times (\hat{n}^q \times \mathbf{E}_b^q) \\ \mathbf{\Lambda}_b^q + \mathbf{\Lambda}_b^s = (\alpha^s + \alpha^q)\hat{n}^s \times (\hat{n}^s \times \mathbf{E}_b^s) \end{cases} \text{ on } \Gamma_{sq}. \quad (7)$$

The choice of α has to satisfy the condition that $\alpha^s + \alpha^q \neq 0$. Note, that by enforcing (7), the tangential electric and magnetic fields are guaranteed to be continuous across the interface Γ_{sq}. Taking the sth subdomain as reference, we can discretize the first equation of (7) to obtain:

$$[N_{bb}^s]_q\{\lambda_b^s\}_q+[L_{bc}^s]_q\{E_c^s\}_q=-[N_{bb}^{sq}]\{\lambda_b^q\}_s -[L_{bc}^{sq}]\{E_c^q\}_s-[M_{bb}^{sq}]\{E_b^q\}_s, \quad (8)$$

where

$$[N_{bb}^s]_q=\iint_{\Gamma_{sq}}\mathbf{N}_b^s\mathbf{N}_b^s dS,$$

$$[L_{bc}^s]_q=\iint_{\Gamma_{sq}}\alpha^s(\hat{n}^s\times\mathbf{N}_b^s)(\hat{n}^s\times\mathbf{N}_c^s)dS,$$

$$[N_{bb}^{sq}]=\iint_{\Gamma_{sq}}\mathbf{N}_b^s\mathbf{N}_b^q dS,$$

$$[L_{bc}^{sq}]=\iint_{\Gamma_{sq}}\alpha^q(\hat{n}^q\times\mathbf{N}_b^s)(\hat{n}^q\times\mathbf{N}_c^q)dS,$$

$$[M_{bb}^{sq}]=\iint_{\Gamma_{sq}}(\alpha^s+\alpha^q)(\hat{n}^q\times\mathbf{N}_b^s)(\hat{n}^q\times\mathbf{N}_b^q)dS.$$

Note, that $[N_{bb}^s]_q$ is always diagonally dominant as long as the same set of basis function is used to expand the auxiliary variable $\mathbf{\Lambda}$ defined on both sides of the shared interface. Therefore, we can take the inversion of $[N_{bb}^s]_q$ to write the transmission condition (8) as:

$$\{\lambda_b^s\}_q+[N_{bb}^s]_q^{-1}[L_{bc}^s]_q[S_q^s]\{E_c^s\} =-[N_{bb}^s]_q^{-1}[N_{bb}^{sq}][T_s^q]\{\lambda_b^q\}-[N_{bb}^s]_q^{-1}[L_{bc}^{sq}][S_s^q]\{E_c^q\} -[N_{bb}^s]_q^{-1}[M_{bb}^{sq}][T_s^q]\{E_b^q\}, \quad (9)$$

where we introduced another two Boolean matrices $[T_q^s]$ and $[S_q^s]$ to extract the unknowns associated with interface Γ_{sq} from those on S_s, such that $\{E_b^s\}_q=[T_q^s]\{E_b^s\}$, $\{\lambda_b^s\}_q=[T_q^s]\{\lambda_b^s\}$, and $\{E_c^s\}_q=[S_q^s]\{E_c^s\}$. Equation (9) can further be simplified by eliminating $\{E_b^q\}$ and the result is:

$$\{\lambda_b^s\}_q+[N_{bb}^s]_q^{-1}([N_{bb}^{sq}][T_s^q]-[M_{bb}^{sq}][T_s^q][F_{bb}^q])\{\lambda_b^q\} +[N_{bb}^s]_q^{-1}[L_{bc}^s]_q[S_q^s][B_c^s]\{E_c\} +[N_{bb}^s]_q^{-1}([L_{bc}^{sq}][S_s^q][B_c^q]-[M_{bb}^{sq}][T_s^q][F_{bc}^q])\{E_c\} =-[N_{bb}^s]_q^{-1}[M_{bb}^{sq}][T_s^q]\{d_r^q\}, \quad (10)$$

where

$$[F_{bb}^q]=[R_{br}^q][K_{rr}^q]^{-1}[R_{br}^q]^{\mathrm{T}}[B_{bb}^q],$$

$$[F_{bc}^q]=[R_{br}^q][K_{rr}^q]^{-1}([K_{rc}^q]+[R_{br}^q]^{\mathrm{T}}[L_{bc}^q])[B_c^q],$$

$$\{d_r^q\}=[R_{br}^q][K_{rr}^q]^{-1}\{f_r^q\}.$$

On one hand, we can assemble (10) over all *s* and *q* to obtain an interface system for all subdomains as:

$$F(\{E_c\},\{\lambda_b\},\{f\})=0. \quad (11)$$

On the other hand, we can assemble the contribution from the primal unknowns (defined on corners) in (6) as:

$$\{E_c\}=G(\{\lambda_b\},\{f\}). \quad (12)$$

By combining (11) and (12) and eliminating $\{E_c\}$, we obtain the nonconformal FETI-DP interface equation for the dual unknowns $\{\lambda_b\}$, which can be solved using a Krylov subspace method. After $\{\lambda_b\}$ is solved, $\{E_c\}$ can be obtained from (12) and the electric field inside each subdomain can be obtained by solving (5).

B. Extension to nonconfomal interface and corner meshes

To further enhance the capability of the LM-based FETI-DP scheme to deal with arbitrary meshes, we now focus on the extension to nonconformal corner cases in this section. Assume that four subdomains share one global corner edge. We denote the number of unknowns defined on each local corner edge as N_c, then call the corner with most unknowns as "master" corner and the others as "slave" corners so that $N_c^{\text{slave}}\le N_c^{\text{master}}$. Note, that subdomains with more than one crosspoint could contain both master and slave corners. We impose the Dirichlet continuity condition at the corner as:

$$\mathbf{E}_t^{\text{master}}=\mathbf{E}_t^{\text{slave}}, \quad (13)$$

in a weak sense, where the subscript *t* specifies the tangential electric field along the corner edge.

The tangential electric field for the master and slave subdomains (taking one slave subdomain for example) can be expanded by two independent sets of basis functions $\{\mathbf{N}_c^{\text{master}}\}$ and $\{\mathbf{N}_c^{\text{slave}}\}$ as:

$$\begin{cases}\mathbf{E}_t^{\text{slave}}=\sum_{n=1}^{N_c^{\text{slave}}}E_{c,\,n}^{\text{slave}}\mathbf{N}_{c,\,n}^{\text{slave}}\\ \mathbf{E}_t^{\text{master}}=\sum_{n=1}^{N_c^{\text{master}}}E_{c,\,n}^{\text{master}}\mathbf{N}_{c,\,n}^{\text{master}}\end{cases}. \quad (14)$$

By substituting (14) into (13) and testing both sides using $\{\mathbf{N}_c^{\text{slave}}\}$, we obtain:

$$[G_{cc}^{\text{slv-slv}}]\{E_c^{\text{slave}}\}=[H_{cc}^{\text{slv-mst}}]\{E_c^{\text{master}}\}, \quad (15)$$

where

$$G_{cc,\,mn}^{\text{slv-slv}}=\int_{\Gamma_c}\mathbf{N}_{c,\,m}^{\text{slave}}\cdot\mathbf{N}_{c,\,n}^{\text{slave}}dl,$$

$$H_{cc,\,mn}^{\text{slv-mst}}=\int_{\Gamma_c}\mathbf{N}_{c,\,m}^{\text{slave}}\cdot\mathbf{N}_{c,\,n}^{\text{master}}dl.$$

Because $[G_{cc}^{\text{slv-slv}}]$ is always diagonal, we have:

$$\{E_c^{\text{slave}}\}=[G_{cc}^{\text{slv-slv}}]^{-1}[H_{cc}^{\text{slv-mst}}]\{E_c^{\text{master}}\}, \quad (16)$$

which means that the corner unknowns defined on the slave corners can be represented by those on the

master corners. Therefore, one can construct a global coarse problem by using only the corner unknowns on all the master corners.

C. Second-order transmission condition

The FOTC employed in Section II.A can be replaced by a higher-order transmission condition to speed up the convergence of the iterative solution of the global interface problem [25-27]. Among them, the SOTC-TE is of particular interest because it can be implemented without introducing any extra auxiliary variables on subdomain interfaces. When incorporated into the dual-primal framework, it does not change the sparsity pattern of the subdomain matrices compared to that in the FOTC case. The subdomain matrix symmetry is also preserved, which is highly desirable for the storage and factorization by a direct sparse solver [34].

For the sth subdomain, the SOTC-TE can be written as:

$$\hat{n}^s \times (\mu_r^{-1} \nabla \times \mathbf{E}^s) + \alpha^s \hat{n}^s \times (\hat{n}^s \times \mathbf{E}^s) - \beta^s \nabla \times [\hat{n}^s (\nabla \times \mathbf{E}^s)_n] = \mathbf{\Lambda}^s \text{ on } S_s, \quad (17)$$

where $(\nabla \times \mathbf{E}^s)_n = \hat{n}^s (\nabla \times \mathbf{E}^s)$ and β^s can be determined based on the smallest mesh size and the order of basis functions on the subdomain interface to account for all the evanescent modes supported by the interface mesh [25,26]. More specifically, $\beta^s = -j/(k_0 + \tilde{k})$, with $\tilde{k} = -j(k_{\max}^2 - k_0^2)^{1/2}$, and $k_{\max} = \pi / h_{\min}$, where $h_{\min}$ denotes the smallest mesh size on the subdomain interface.

Adding the transmission conditions from two neighboring subdomains and eliminating the tangential magnetic field, we have:

$$\begin{cases} \mathbf{\Lambda}_b^s + \mathbf{\Lambda}_b^q = (\alpha^s + \alpha^q)\hat{n}^q \times (\hat{n}^q \times \mathbf{E}_b^q) \\ \qquad - (\beta^s + \beta^q) \nabla \times [\hat{n}^q (\nabla \times \mathbf{E}_b^q)_n], \\ \mathbf{\Lambda}_b^q + \mathbf{\Lambda}_b^s = (\alpha^s + \alpha^q)\hat{n}^s \times (\hat{n}^s \times \mathbf{E}_b^s) \\ \qquad - (\beta^s + \beta^q) \nabla \times [\hat{n}^s (\nabla \times \mathbf{E}_b^s)_n] \end{cases} \quad (18)$$

on Γ_{sq}. It can be seen that in addition to the Dirichlet and Neumann continuity conditions, the SOTC-TE also enforces the continuity of $\nabla \times [\hat{n}(\nabla \times \mathbf{E})_n]$, which is related to the tangential variation of the normal magnetic flux density. Due to the use of the SOTC-TE, the computation of some matrices in Section II.A has to be modified as follows:

$$[M_{bb}^s] = \iint_{S_s} [\alpha^s (\hat{n}^s \times \mathbf{N}_b^s)(\hat{n}^s \times \mathbf{N}_b^s) + \beta^s (\nabla \times \mathbf{N}_b^s)_n (\nabla \times \mathbf{N}_b^s)_n] dS,$$

$$[L_{bc}^s] = \iint_{S_s} [\alpha^s (\hat{n}^s \times \mathbf{N}_b^s)(\hat{n}^s \times \mathbf{N}_c^s) + \beta^s (\nabla \times \mathbf{N}_b^s)_n (\nabla \times \mathbf{N}_c^s)_n] dS,$$

$$[L_{bc}^s]_q = \iint_{\Gamma_{sq}} [\alpha^s (\hat{n}^s \times \mathbf{N}_b^s)(\hat{n}^s \times \mathbf{N}_c^s) + \beta^s (\nabla \times \mathbf{N}_b^s)_n (\nabla \times \mathbf{N}_c^s)_n] dS,$$

$$[L_{bc}^{sq}] = \iint_{\Gamma_{sq}} [\alpha^q (\hat{n}^q \times \mathbf{N}_b^s)(\hat{n}^q \times \mathbf{N}_c^q) + \beta^q (\nabla \times \mathbf{N}_b^s)_n (\nabla \times \mathbf{N}_c^q)_n] dS,$$

$$[M_{bb}^{sq}] = \iint_{\Gamma_{sq}} (\alpha^s + \alpha^q)(\hat{n}^q \times \mathbf{N}_b^s)(\hat{n}^q \times \mathbf{N}_b^q) + (\beta^s + \beta^q)(\nabla \times \mathbf{N}_b^s)_n (\nabla \times \mathbf{N}_b^q)_n] dS.$$

D. Hybrid nonconformal FETI/conformal FETI-DP

For the multi-region domain decomposition, when a subdomain interface resides within one region, it must be mesh-conformal and geometry-conformal. In this case, $[B_{bb}^s]$ in Section II.A is reduced to a projection Boolean matrix, $[N_{bb}^s]_q$ and $[N_{bb}^{sq}]$ become identity matrices, and one does not have to deal with projections on the geometrical crosspoints as described in Section II.B. Thus, it is necessary to design an efficient hybrid algorithm to take advantage of the partially conformal meshes.

For this, we propose a general crosspoint correction technique to ensure good accuracy, fast convergence, and a nonsingular global interface matrix [33,34]. The basic idea includes the following guidelines: (1) the Lagrange multipliers need to be split into two when they are defined on the edges connecting an inter-region interface and an interior interface within one region. (2) By automatic domain decomposition, it is possible to have geometry crosspoints sitting on an inter-region interface. If this is the case, convert the original corner unknowns into non-corner interface unknowns, define Lagrange multipliers on these crosspoints and split each Lagrange multiplier into two. (3) In geometry-nonconformal cases, one Lagrange multiplier may be shared by more than two neighboring subdomains. In this case, split such a Lagrange multiplier according to the number of overlapped neighboring subdomains and let each Lagrange multiplier after splitting take care of the communication from the reference subdomain to each neighboring subdomain.

Actually, Guidelines 1 and 2 are two special cases described by Guideline 3. It should be noted that splitting Lagrange multiplier introduces extra boundary unknowns into the original global interface problem, which may lead to a singular global interface matrix equation. For this, a corner penalty term technique is employed to remove the singularity or near singularity due to the redundancy [27].

III. NUMERICAL EXAMPLES

The algorithms described in Section II have been implemented on different serial and parallel computing platforms. In this section, we present several numerical examples to demonstrate their accuracy and convergence performance. For antenna array simulations, the repetition of the array structure is fully exploited in order to save time for generating the mesh and factorizing repeated subdomain matrices.

A. Vivaldi antenna array

The first example is designed to explore the capability of the LM-based FETI-DP method to analyze large-scale antenna arrays, and compare its performance to that of the FETI-DPEM2 [11] and the Cement-Element (CE)-based FETI-DP method [18]. The size of the simulated Vivaldi antenna array increases from 3×3 to 100×100. To truncate the computational domain, the first-order ABC is placed at one extra unit cell surrounding the array in the xy-plane. The distance between two adjacent elements in both the x- and y-directions is set to be 36 mm. Figure 1 (a) shows the Vivaldi antenna element, where the height, width, and thickness of the substrate are d=33.3 mm, w=34.0 mm, and h=1.27 mm, respectively. The lossless substrate has a relative permittivity of 6.0. The radius of the hollow circle is chosen to be R=2.5 mm. The half-width of the slot line varies with z according to an exponential function given by $w(z)$=0.25exp(0.123z) mm. This function gives a half-width of 15 mm at the open mouth. The antenna is fed by a coaxial line with an inner radius r_{in}=0.375 mm and an outer radius r_{out}=0.875 mm from under the ground. A 5-mm coaxial line is modeled and then terminated with a waveguide port boundary condition with only the TEM mode assumed at the end of the coax.

The convergence history of the iterative solution of the global interface problem for the 100×100 array simulated by the conformal, LM-based, and CE-based FETI-DP methods is plotted in Fig. 1 (a), and the computed radiation patterns are compared in Figs. 1 (b) and 1 (c). The BiCGStab iterative solver is employed with a stopping criterion of 10^{-3}. For this array, the LM- and CE-based FETI-DP methods have a similar convergence behavior and yield nearly identical results to that of the conformal FETI-DP method.

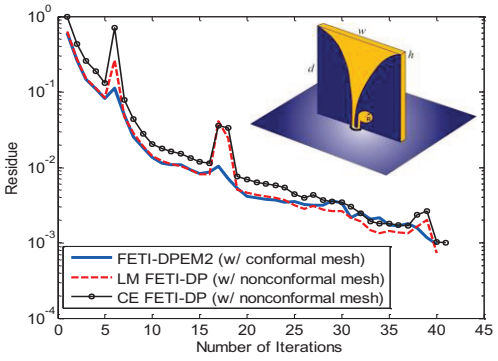

(a)

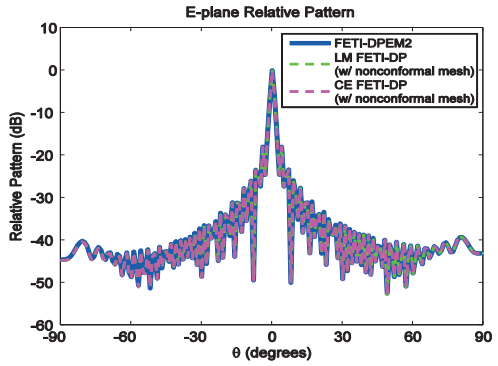

(b)

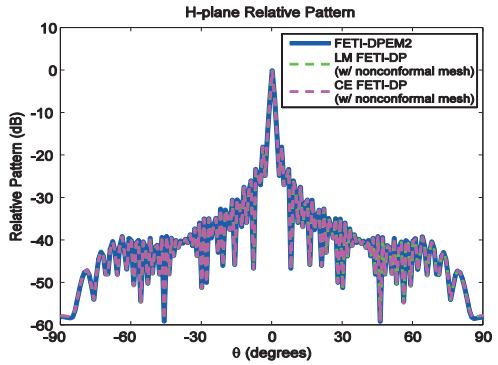

(c)

Fig. 1. Simulation of the 100 × 100 Vivaldi antenna array at 3 GHz. (a) Convergence history, (b) broadside scan E-plane relative pattern, and (c) broadside scan H-plane relative pattern.

In Table 1, we list the computation resources used to simulate Vivaldi antenna arrays of different sizes by the LM-based FETI-DP method. All examples are run on an HP workstation, equipped with a 2.66-GHz Intel Xeon processor and 12 GB memory. To plot the scalability curve as shown in Fig. 2, we record the computation time for solving the global interface dual unknowns as well as the total computation time. It is observed that the computation time increases linearly with the total number of unknowns in this case.

Table 1: Computational information of the nonconformal FETI-DP method for simulating various Vivaldi antenna arrays. The computation time is in the hour:minute:second format

Array Size	# of Unknowns	Interface Time (# of Iterations)	Total Time
3×3	209,792	00:00:21 (28)	00:02:20
10×10	1,908,552	00:04:54 (44)	00:13:43
31×31	17,410,080	00:49:27 (51)	02:01:21
100×100	178,235,832	07:19:58 (40)	19:32:20

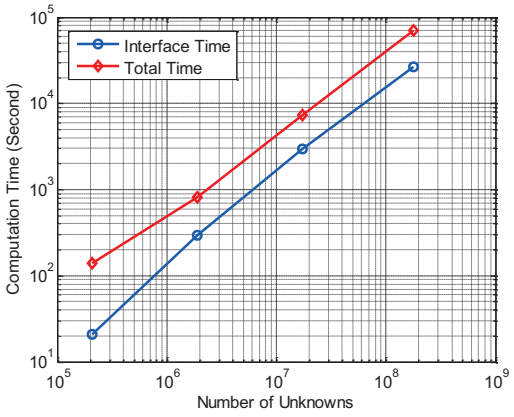

Fig. 2. Computation time as a function of the total number of unknowns for various Vivaldi antenna arrays.

Antenna array is a typical case where the outgoing wave may propagate towards the truncation boundary at an oblique direction. If this is the case, no matter how far away the ABC is placed, its absorption is limited and the artificial reflection may not be reduced to a desired level. To effectively reduce the artificial reflection, we can employ an oblique ABC as [36]:

$$\hat{n}\times(\nabla\times\mathbf{E}) = -jk_0\cos\theta_s\hat{n}\times(\hat{n}\times\mathbf{E}) + (jk_0/\cos\theta_s)\hat{t}(\hat{t}\mathbf{E}), \quad (19)$$

where $\hat{t} = (\hat{\phi}_s\times\hat{n})\sin\theta_s\cos\phi_s + \hat{\phi}_s\sin\theta_s\sin\phi_s$ and $\hat{n}$ denotes the outward unit normal vector of the planar truncation surface. The angle for perfect absorption of this ABC can be tuned by parameters θ_s and ϕ_s. Obviously, (19) is reduced to the conventional ABC if $\theta_s = 0^o$. Therefore, we can always tune this ABC to minimize the reflection error for the analysis of large finite phased arrays as long as the direction of the main beam of the radiated wave is specified.

To investigate the performance of the oblique ABC, a 20×20 Vivaldi antenna array is considered. For the mesh truncation of the upper half space, we have two setups. One is a hemispherical surface with a base radius of 7λ, whereas the other is a rectangular surface placed 1λ away from both the top and the side of the antenna array. The size of the rectangular box is $8.8\lambda\times9.2\lambda\times1.33\lambda$. Apparently, the second setup is computationally more efficient than the first one because its computational domain is much smaller. However, in the second setup, the radiated field will be incident on the top truncation surface at a much larger angle than in the first one if the antenna array is set to radiate away from broadside. In this case, the oblique ABC can provide a good absorption performance while minimizing the size of the computational domain. The 20×20 Vivaldi antenna array is simulated at 3.0 GHz using: (1) the conventional ABC with the hemispherical truncation surface, (2) the conventional ABC with the rectangular truncation surface, and (3) the oblique ABC with the rectangular truncation surface for the main beam (θ_s,ϕ_s) steered to $(60^o,0^o)$. The near-zone field distributions in the *yz*-plane are plotted in Fig. 3. We take the result of Case 1 shown in Fig. 3 (a) as the reference solution and enlarge the portion close to the antenna array in Fig. 3 (b) for a better comparison between the results of Cases 2 and 3, which are shown in Figs. 3 (c) and 3 (d). For the case of $(\theta_s,\phi_s) = (60^o,0^o)$, Case 3 yields a visually much better result than does Case 2, as shown in Figs. 3 (c) and 3 (d). The far-field radiation patterns calculated in the three cases above are compared in Fig. 4, which shows that the result of

Case 2 deviates from the reference solution by 3 dB, whereas the result of Case 3 has a much smaller derivation. For Cases 2 and 3, it takes 9.2 minutes to finish the simulation of one frequency point on one computational node which contains 16 Intel Xeon 2.70-GHz processors. The result of the reference case (Case 1) is obtained using the hybrid conformal/nonconformal domain decomposition solver described in Section II.D with 43.5 minutes for one frequency on the same node.

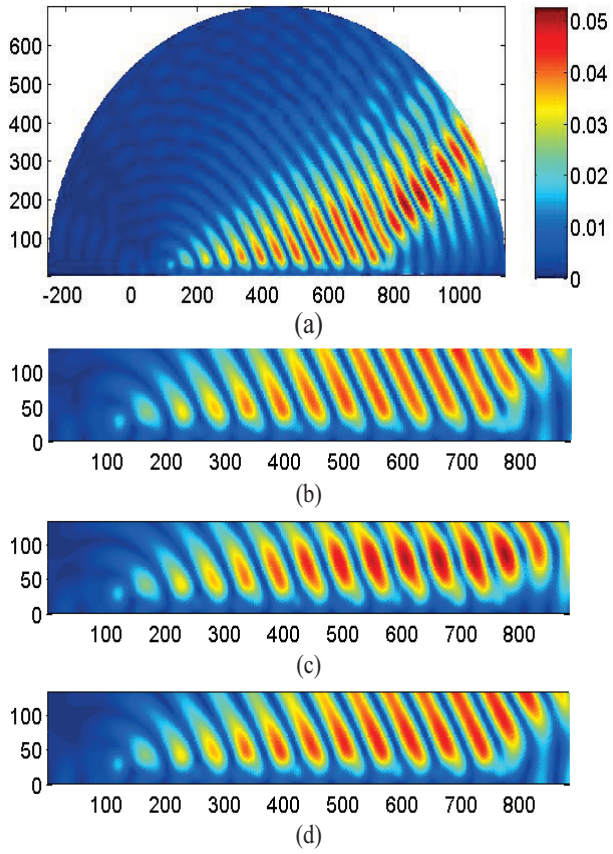

Fig. 3. $|\mathrm{Re}(E)|$ for the 20×20 Vivaldi antenna array in the *xz*-plane at 3.0 GHz with steering angle set at $(\theta_s,\phi_s)=(60^\circ,0^\circ)$. (a) Computed using the conventional ABC with a hemispherical truncation surface, (b) same as (a) but plotted in a limited region for the purpose of comparison, (c) computed using the conventional ABC with a rectangular truncation surface, and (d) computed using the oblique ABC with a rectangular truncation surface.

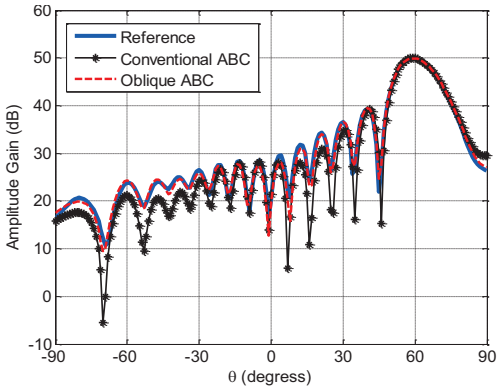

Fig. 4. Co-polarized radiation patterns for the 20×20 Vivaldi antenna array in the *xz*-plane at 3.0 GHz when the main beam is steered to $(\theta_s,\phi_s)=(60^\circ,0^\circ)$.

B. NRL Vivaldi antenna array with a radome

In this example, we consider the near-field interaction between a phased-array antenna and its surrounding environment. The antenna array adopted was designed by the Naval Research Lab (NRL) [37]. A radome is placed on the top of the array for mechanical protection. The hybrid nonconformal FETI/conformal FETI-DP method is employed to solve this multi-region problem.

In the 11 × 11 dual-polarized array, each Vivaldi antenna element consists of three layers of metal printed on a dielectric substrate with a height of 246.253 mm, a width of 35.56 mm, and a thickness of 3.3274 mm. The relative permittivity of the dielectric slab is $\varepsilon_r=2.2-j0.0009$. The metallic layers are equally spaced and are connected by vias with a radius of 0.79 mm. All antenna elements are connected to each other by solid metal posts and mounted vertically on a finite ground whose size is 528 mm × 528 mm. For more geometrical details, the reader is referred to [37].

At 3.02 GHz, the hemispherical radome has a base radius of 5.5λ. The thickness and the relative permittivity of the radome are 0.1λ and $\varepsilon_r=2.0-j1.0$, respectively. The conventional first-order ABC is used on a hemispherical surface placed 1λ away from the exterior boundary of the hemispherical radome. In this case, the first-order ABC is a better choice because the truncation

surface can be made conformal to the radome to reduce the size of the computational domain. In addition, it provides good absorption for waves radiating along any direction. Figure 5 shows the radiation patterns of the array with and without the radome. All radiation patterns are normalized by the value in the maximum radiation direction of the array without the radome. It can be seen that due to the loss of the radome, the emitted power in the main beam direction is reduced by around 3 dB. The result using conformal meshes on the inter-region interfaces is also plotted for comparison. Apparently, using nonconformal inter-region interface meshes does not sacrifice the accuracy of the solution since two sets of data are on the top of each other. The field distribution is also plotted in Fig. 6 for the cases with and without the radome. Finally, the convergence history the iterative solution of the global interface problem for the array with the radome is given in Fig. 7. It should be noted that for large-scale problems, the nonconformal meshes on the interfaces between different regions may introduce some numerical resonance and yield slower convergence than a conformal mesh does.

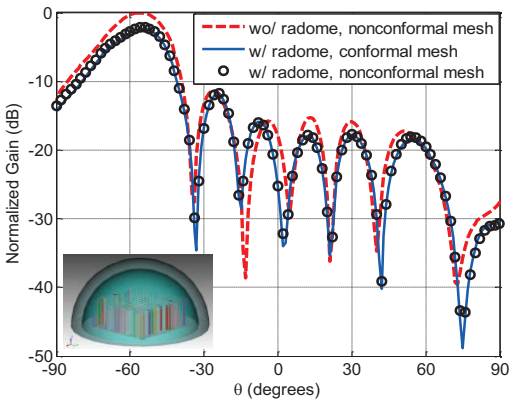

Fig. 5. Comparison between the radiation patterns for the array with and without the radome at 3.02 GHz and steering angle $\theta_s = -60^\circ$ and $\phi_s = 0^\circ$.

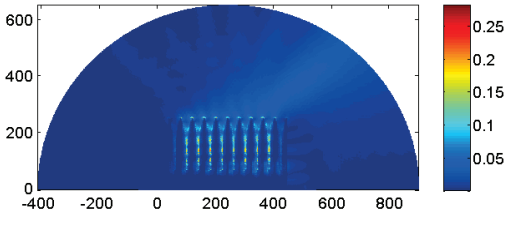

(a)

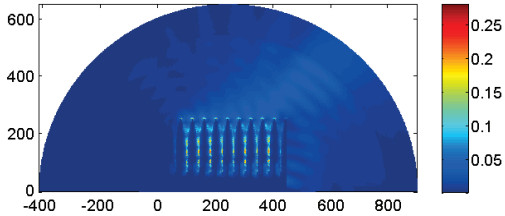

(b)

Fig. 6. $|E|$ in the $\phi = 0^\circ$ plane for H-pol excitation at 3.02 GHz and steering angle $\theta_s = 60^\circ$ and $\phi_s = 0^\circ$. (a) The NRL array itself, and (b) the NRL array with a radome.

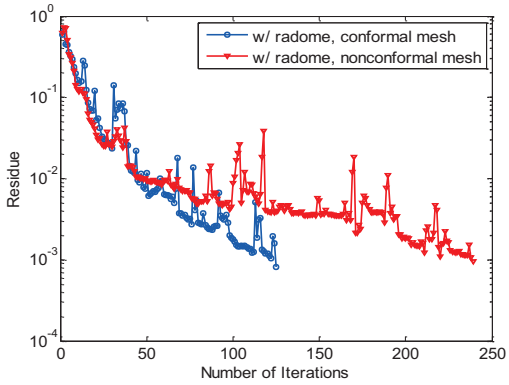

Fig. 7. Convergence history of the iterative solution of the global interface problem for the NRL array with the radome.

C. Subwavlength wave guiding and focusing

As the last example, we simulate a taper transition device which can guide waves from a wavelength-scale transmission line to a subwavelength-scale one. The basic structure is a periodic arrangement of metallic bricks standing on a metallic surface, as shown in Fig. 8 (a). The period of each brick-groove pair is $d = \lambda/8 = 0.2$ mm, the length and height of each metallic brick are $l = 0.5d$ and $h = 1.5d$, and the width shrinks from $w_{\text{in}} = 16d$ to $w_{\text{out}} = 0.5d$ linearly through an 18-period transition. The input and output ports of the entire device are connected to the taper structure by 12- and 18-period uniform waveguides, respectively. The entire structure is made of aluminum, which has $\varepsilon_r = -3.39 \times 10^4 - j3.5 \times 10^6$ at $\lambda = 1.6$ mm. At this frequency, the aluminum can also be modeled as a Perfect Electric Conductor (PEC), because the modal effective index as a function of w for a PEC

is almost the same as that for the aluminum [38]. In the simulation, the grating lies on an infinitely large ground plane, which is also modeled as a PEC. To excite the fundamental TM-like mode whose magnetic field is parallel to the groove orientation, a current sheet is placed perpendicularly to the wave propagation direction at the input port. The ABC or PML truncation is placed one wavelength away from the top and four sides of the device. In this paper, we implement the PML as a diagonally anisotropic artificial medium, with $\ddot{\mu}_r = \mu_r[D]$ and $\ddot{\varepsilon}_r = \varepsilon_r[D]$, where:

$$[D] = \begin{bmatrix} a & 0 & 0 \\ 0 & b & 0 \\ 0 & 0 & c \end{bmatrix}. \tag{20}$$

The diagonal entries of $[D]$ can be further written as $a = s_y s_z / s_x$, $b = s_z s_x / s_y$, and $c = s_x s_y / s_z$, where s_x, s_y, and s_z are functions of spatial variables x, y, and z, respectively. In the PML region, s_x, s_y, and s_z can be expressed as $s_a = s' - js''$, where a could be x, y, or z, and s' and s'' are real numbers with $s' \geq 1$ and $s'' \geq 0$, which are used to control the attenuation of the evanescent and propagating waves in the PML [1].

To compare the convergence performance of the FETI-DP method with the SOTC-TE when the computational domain is truncated using either the ABC or the PEC-back PML, we discretize the entire computational domain with the same mesh, reset the material properties of the tetrahedral elements in the PML region, and change the boundary condition at the exterior boundary. With this, the number of unknowns using two different truncations remains roughly the same. When the entire computational domain is divided into 512 subdomains, there are 3,342,990 primal unknowns, 724,544 dual unknowns, and 22,933 corner unknowns for the ABC truncation, whereas those for the PML truncation are 3,302,780, 719,112, and 22,932, respectively. Figure 8 (b) shows the simulated electric field intensity distribution in the plane 30 μm above the waveguide. As can be seen, when propagating in the taper, the mode size becomes smaller and smaller with a gradually increased intensity, which demonstrates the wave squeezing and focusing phenomenon observed in the experiment [38]. The convergence history of the iterative solution of the global interface problem using the FETI-DP method with the SOTC-TE and the cement element method with the SOTC-FULL [26] is given in Fig. 9 for both the ABC and PML truncations. In both cases, the FETI-DP method outperforms the cement element method in terms of iteration steps. Also, the convergence does not slow down too much when the ABC is replaced with the PML.

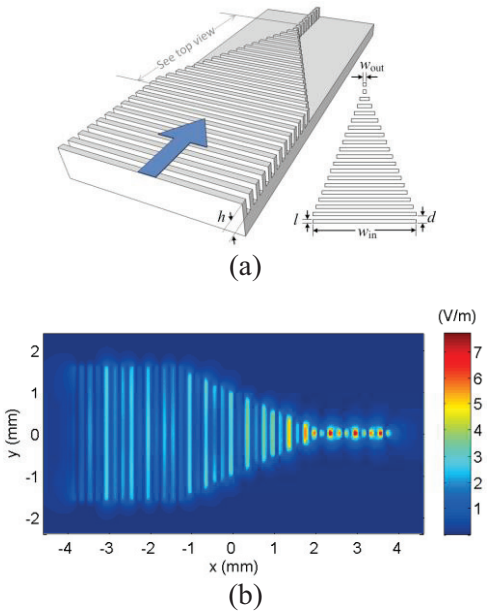

Fig. 8. Subwavelength waveguiding and focusing device. (a) Geometry; the waveguide width transits from $L_{in} = 16d$ to $L_{out} = 0.5d$ after 18 periods, and (b) electric field in the plane 30 μm above the waveguide.

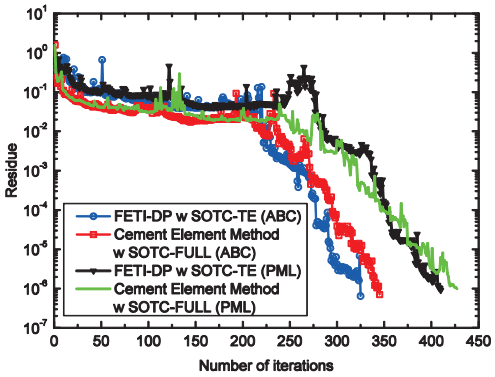

Fig. 9. Convergence history of the iterative solution of the global interface problem when the computational domain is truncated by ABC and PEC-backed PML.

IV. CONCLUSION

In this paper, we presented an overview of our recent effort on the domain decomposition finite element analysis of large-scale electromagnetic problems. First, we described the formulation of the LM-based FETI-DP method to deal with nonconformal interface and corner meshes. Then we discussed an approach to employ a higher-order transmission condition to improve the convergence performance of the interface iterative solution. Afterwards, we introduced a hybrid nonconformal FETI/conformal FETI-DP scheme to model multi-region electromagnetic problems, which relies on a general corner correction technique to handle mesh-nonconformal and geometry-nonconformal meshes on the inter-region interface. Finally, we gave a few numerical examples to demonstrate the finite element analysis of various antenna arrays, where we employed an oblique ABC designed for absorbing waves radiating from an array. In addition, we validated the PML mesh truncation through the simulation of a wave-guiding and focusing device. The application examples demonstrated that the finite element-based DDM is a powerful numerical simulation technique for the analysis of large-scale electromagnetic problems.

REFERENCES

[1] J. M. Jin, "The finite element method in electromagnetics," 2nd edition, *Wiley*, New York, 2002.

[2] A. Toselli and O. Widlund, "Domain decomposition methods-algorithms and theory," *Springer-Verlag*, Berlin, 2005.

[3] B. Després, P. Joly, and J. E. Roberts, "A domain decomposition method for the harmonic maxwell equations," *In Iterative Methods In Linear Algebra*, North-Holland, Amsterdam, pp. 475-484, 1992.

[4] B. Stupfel and M. Mognot, "A domain decomposition method for the vector wave equation," *IEEE Trans. Antennas Propag*., vol. 48, no. 5, pp. 653-660, May 2000.

[5] C. Farhat and F. Roux, "A method of finite element tearing and interconnecting and its parallel solution algorithm," *Int. J. Numer. Meth. Eng*., vol. 32, no. 6, pp. 1205-1227, October 1991.

[6] C. Farhat, A. Macedo, M. Lesoinne, F. X. Roux, and F. Magoulès, "Two-level domain decomposition methods with lagrange multipliers for the fast iterative solution of acoustic scattering problems," *Comput. Methods Appl. Mech. Eng*., vol. 184, no. 2-4, pp. 213-239, April 2000.

[7] C. Farhat, M. Lesoinne, P. LeTallec, K. Pierson, and D. Rixen, "FETI-DP: a dual-primal unified FETI method-part I: a faster alternative to the two-level FETI method," *Int. J. Numer. Meth. Eng*., vol. 50, no. 7, pp. 1523-1544, March 2001.

[8] C. Farhat, J. Li, and P. Avery, "A FETI-DP method for the parallel iterative solution of indefinite and complex-valued solid and shell vibration problems," *Int. J. Numer. Meth. Eng.*, vol. 63, no. 3, pp. 398-427, May 2005.

[9] C. Farhat, P. Avery, R. Tezaur, and J. Li, "FETI-DPH: a dual-primal domain decomposition method for acoustic scattering," *J. Comput. Acoust*., vol. 13, no. 3, pp. 499-524, March 2005.

[10] Y. J. Li and J. M. Jin, "A vector dual-primal finite element tearing and interconnecting method for solving 3D large-scale electromagnetic problems," *IEEE Trans. Antennas Propag*., vol. 54, no. 10, pp. 3000-3009, October 2006.

[11] Y. J. Li and J. M. Jin, "A new dual-primal domain decomposition approach for finite element simulation of 3D large-scale electromagnetic problems," *IEEE Trans. Antennas Propag*., vol. 55, no. 10, pp. 2803-2810, October 2007.

[12] Y. J. Li and J. M. Jin, "Implementation of the second-order ABC in the FETI-DPEM method for 3D EM problems," *IEEE Trans. Antennas Propag*., vol. 56, no. 8, pp. 2765-2769, August 2008.

[13] S. C. Lee, M. N. Vouvakis, and J. F. Lee, "A non-overlapping domain decomposition method with non-matching grids for modeling large finite antenna arrays," *J. Comput. Phys*., vol. 203, no. 1, pp. 1-21, February 2005.

[14] M. N. Vouvakis, Z. Cendes, and J. F. Lee, "A FEM domain decomposition method for photonic and electromagnetic band gap structures," *IEEE Trans. Antennas Propag*., vol. 54, pp. 721-733, February 2006.

[15] K. Zhao, V. Rawat, S. C. Lee, and J. F. Lee, "A domain decomposition method with nonconformal meshes for finite periodic and semi-periodic structures," *IEEE Trans. Antennas Propag*., vol. 55, no. 9, pp. 2559-2570, September 2007.

[16] Z. Q. Lu, X. An, and W. Hong, "A fast domain decomposition method for solving three-dimensional large-scale electromagnetic problems," *IEEE Trans. Antennas Propag*., vol. 56, no. 8, pp. 2200-2210, August 2008.

[17] M. F. Xue and J. M. Jin, "Application of a nonconformal FETI-DP method in antenna array simulations," *In IEEE APS Int. Symp. Dig*., pp. 1-2, July 2012.

[18] M. F. Xue and J. M. Jin, "Nonconformal FETI-DP methods for large-scale electromagnetic simulation," *IEEE Trans. Antennas Propag*., vol. 60, no. 9, pp. 4291-4305, September 2012.

[19] M. J. Gander, F. Magoulès, and F. Nataf, "Optimized schwarz methods without overlap for the helmholtz equation," *SIAM J. Sci. Comput*., vol. 24, no. 1, pp. 38-60, 2003.

[20] M. J. Gander, L. Halpern, and F. Magoulès, "An optimized schwarz method with two-sided robin transmission conditions for the helmholtz equation," *Int. J. Numer. Meth. Fluids*, vol. 55, no. 2, pp. 163-175, September 2007.

[21] M. J. Gander and F. Kwok, "Best robin parameters for optimized schwarz methods at cross points," *SIAM J. Sci. Comput*., vol. 34, no. 4, pp. 1849-1879, 2010.

[22] P. Collino, G. Delbue, P. Joly, and A. Piacentini, "A new interface condition in the non-overlapping domain decomposition for the maxwell equations," *Comput. Methods Appl. Mech. Eng*., vol. 148, no. 1-2, pp. 195-207, August 1997.

[23] A. Alonso-Rodriguez and L. Gerardo-Giorda, "New nonoverlapping domain decomposition methods for the harmonic maxwell system," *SIAM J. Sci. Comput*., vol. 28, no. 1, pp. 102-122, 2006.

[24] V. Dolean, M. J. Gander, and L. Gerardo-Giorda, "Optimized schwarz methods for maxwell's equations," *SIAM J. Sci. Comput*., vol. 31, no. 3, pp. 2193-2213, 2009.

[25] Z. Peng, V. Rawat, and J. F. Lee, "One way domain decomposition method with second order transmission conditions for solving electromagnetic wave problems," *J. Comput. Phys*., vol. 229, no. 4, pp. 1181-1197, February 2010.

[26] Z. Peng and J. F. Lee, "Non-conformal domain decomposition method with second-order transmission conditions for time-harmonic electromagnetics," *J. Comput. Phys*., vol. 229, no. 8, pp. 5615-5629, August 2010.

[27] Z. Peng and J. F. Lee, "Non-conformal domain decomposition method with mixed true second order transmission condition for solving large finite antenna arrays," *IEEE Trans. Antennas Propag*., vol. 59, no. 5, pp. 1638-1651, May 2011.

[28] J. Ma, J. M. Jin, and Z. Nie, "A nonconformal FEM-DDM with tree-cotree splitting and improved transmission condition for modeling subsurface detection problems," *IEEE Trans. Geosci. Remote Sens*., vol. 52, no. 1, pp. 355-364, January 2014.

[29] A. F. Peterson, "Absorbing boundary conditions for the vector wave equation," *Microwave Opt. Technol. Lett*., vol. 1, no. 2, pp. 62-64, April 1988.

[30] J. P. Webb and V. N. Kanellopoulos, "Absorbing boundary conditions for the finite element solution of the vector wave equation," *Microwave Opt. Technol. Lett*., vol. 2, no. 10, pp. 370-372, October 1989.

[31] B. Stupfel, "Numerical implementation of second- and third-order conformal absorbing boundary conditions for the vector-wave equation," *IEEE Trans. Antennas Propag*., vol. 45, no. 3, pp. 487-492, March 1997.

[32] Q. He and D. Jiao, "A rigorous divide-and-conquer algorithm for fast DC-mode extraction," in *IEEE APS Int. Symp. Dig*., pp. 1630-1631, July 2013.

[33] M. F. Xue and J. M. Jin, "A hybrid nonconformal FETI/conformal FETI-DP method for arbitrary nonoverlapping domain decomposition modeling," *In IEEE APS Int. Symp. Dig*., pp. 1628-1629, July 2013.

[34] M. F. Xue and J. M. Jin, "A hybrid conformal/ nonconformal domain decomposition method for multi-region electromagnetic modeling," *IEEE Trans. Antennas Propag*., in press.

[35] J. P. Webb, "Hierarchical vector basis functions of arbitrary order for triangular and tetrahedral elements," *IEEE Trans. Antennas Propag*., vol. 47, no. 8, pp. 1244-1253, August 1999.

[36] M. F. Xue and J. M. Jin, "Application of an oblique absorbing boundary condition in the finite element simulation of phased-array antennas," *Microwave Opt. Technol. Lett*., vol. 56, no. 1, pp. 178-184, January 2014.

[37] M. F. Xue, J. M. Jin, S. Wong, C. Macon, and M. Kragalott, "Experimental validation of the FETI-DPEM algorithm for simulating phased-array antennas," *In IEEE APS Int. Symp. Dig*., pp. 2495-2498, July 2011.

[38] W. Zhao, O. M. Eldaiki, R. Yang, and Z. Lu, "Deep subwavelength waveguiding and focusing based on designer surface plasmons," *Opt. Express*, vol. 18, no. 20, pp. 21498-21503, September 2010.

Ming-Feng Xue received the B.S. degree in Electronic Information Engineering from Anhui University, Hefei, China, in 2005, and the M.S. degree in Electromagnetic Field and Microwave Technology from Shanghai Jiao Tong University, Shanghai, China, in 2008, respectively. He is currently working towards the Ph.D. degree in Electrical and Computer Engineering at the University of Illinois at Urbana-Champaign.

Since 2008, he has been a Research Assistant with the Center for Computational Electromagnetics at the University of Illinois at Urbana-Champaign. His research interests include finite element boundary integral methods, domain decomposition methods, and parallel electromagnetics simulation.

Jian-Ming Jin joined the University of Illinois at Urbana-Champaign in 1993 and is currently the Y. T. Lo Chair Professor of Electrical and Computer Engineering, and Director of the Electromagnetics Laboratory and Center for Computational Electromagnetics. He has authored and co-authored over 200 papers in refereed journals and 20 book chapters. He has also authored The Finite Element Method in Electromagnetics (Wiley, 1st edition 1993, 2nd edition 2002), Electromagnetic Analysis and Design in Magnetic Resonance Imaging (CRC, 1998), Theory and Computation of Electromagnetic Fields (Wiley, 2010), and co-authored Computation of Special Functions (Wiley, 1996), Fast and Efficient Algorithms in Computational Electromagnetics (Artech, 2001), and Finite Element Analysis of Antennas and Arrays (Wiley, 2008). His current research interests include computational electromagnetics, scattering and antenna analysis, electromagnetic compatibility, high-frequency circuit modeling and analysis, bioelectromagnetics, and magnetic resonance imaging. He was elected by ISI as one of the world's most cited authors in 2002.